

**ROBUST AND SCALABLE NONLINEAR SOLVERS FOR FINITE  
ELEMENT DISCRETIZATIONS OF BIOLOGICAL  
TRANSPORTATION NETWORKS**

JAN HASKOVEC <sup>1</sup>

PETER MARKOWICH <sup>1,2</sup>

SIMONE PORTARO <sup>1,3</sup>

STEFANO ZAMPINI <sup>1</sup>

<sup>1</sup>*King Abdullah University of Science and Technology  
Thuwal 23955-6900, Kingdom of Saudi Arabia*

<sup>2</sup>*Faculty of Mathematics, University of Vienna,  
Oskar-Morgenstern-Platz 1, 1090 Vienna*

<sup>3</sup>*Dipartimento di Ingegneria e Scienze dell'Informazione e Matematica (DISIM)  
Università degli Studi dell'Aquila*

**ABSTRACT.** We develop robust and scalable fully implicit nonlinear finite element solvers for the simulations of biological transportation networks driven by the gradient flow minimization of a non-convex energy cost functional. Our approach employs a discontinuous space for the conductivity tensor that allows us to guarantee the preservation of its positive semi-definiteness throughout the entire minimization procedure arising from the time integration of the gradient flow dynamics using a backward Euler scheme. Extensive tests in two and three dimensions demonstrate the robustness and performance of the solver, highlight the sensitivity of the emergent network structures to mesh resolution and topology, and validate the resilience of the linear preconditioner to the ill-conditioning of the model. The implementation achieves near-optimal parallel scaling on large-scale, high-performance computing platforms. To the best of our knowledge, the network formation system has never been simulated in three dimensions before. Consequently, our three-dimensional results are the first of their kind.

---

*E-mail addresses:* {jan.haskovec, peter.markowich, stefano.zampini}@kaust.edu.sa,  
peter.markowich@univie.ac.at, simone.portaro@univaq.it.

## 1. INTRODUCTION

A transportation network can be understood as a spatial configuration that facilitates the movement or transfer of various resources. In biological systems, network structures such as leaf venation patterns, vascular systems, and neural connections have garnered considerable attention in recent research [10, 16, 18, 36]. A key area of study focuses on optimizing transport properties—whether electrical, fluid-based, or material flows—by balancing competing factors such as cost, transport efficiency, and resilience to failure [15]. Unlike engineered networks, biological transportation systems evolve without centralized control [50]. Instead, they are shaped by numerous cycles of evolutionary adaptation, making them prime examples of emergent structures governed by self-regulating processes.

This paper investigates a class of self-regulating processes governed by the minimization of a biological energy cost functional given by

$$(1) \quad E[\mathbb{C}] = \int_{\Omega} \left( c^2 \nabla p \cdot (\mathbb{C} + r\mathbb{I}) \nabla p + \frac{\nu}{\gamma} \left( \|\mathbb{C}\|^2 + \varepsilon \right)^{\frac{\gamma}{2}} \right) dx,$$

where  $\mathbb{C}(x)$  is a symmetric, positive semi-definite (SPSD) conductivity tensor defined on an open, bounded domain  $\Omega \subset \mathbb{R}^d$  (with  $d = 2, 3$  for physical applications). The scalar field  $p(x)$  represents the material pressure in a porous medium, and it is assumed to obey a Darcy law

$$(2) \quad -\nabla \cdot ((\mathbb{C} + r\mathbb{I}) \nabla p) = S, \quad \text{in } \Omega,$$

where  $S(x)$  represents a prescribed spatial distribution of sources and sinks of material. The parameter  $c$  quantifies the system's propensity to align with the pressure gradient,  $r > 0$  describes the isotropic background permeability of the medium,  $\nu > 0$  denotes the metabolic constant,  $\gamma > 0$  is the metabolic exponent, and  $\varepsilon > 0$  is a regularization parameter. In biological contexts, such as plant leaf venation, the metabolic exponent typically falls within  $1/2 \leq \gamma \leq 1$ , as shown in [34, 35]. In contrast, for blood vessels, metabolic costs are proportional to the vessel's cross-sectional area, implying  $\gamma = 1/2$ , see [43]. The notation  $\|\cdot\|$  refers to the Frobenius norm, although other norms may be considered depending on the specific context or application of interest. We emphasize that setting  $\varepsilon = 0$  recovers the metabolic term originally introduced in [34, 35].

Evolutionary selection is modeled as the minimization of the energy functional eq. (1) subject to the constraint eq. (2) with respect to  $\mathbb{C}$ . To be able to study the formation and, eventually, adaptation of the network patterns, we consider the formal  $L^2$ -gradient flow of the constrained energy functional eq. (1)–eq. (2),

$$(3) \quad \frac{\partial \mathbb{C}}{\partial t} = c^2 \nabla p \otimes \nabla p - \nu \left( \|\mathbb{C}\|^2 + \varepsilon \right)^{\frac{\gamma-2}{2}} \mathbb{C} \quad \text{in } \Omega \times [0, \infty),$$

where  $t \geq 0$  is a time-like variable associated with the gradient flow dynamics; see [29]. We assume that the source term  $S = S(x)$  remains constant in time; time-varying sources can be accommodated by adding an extra first-order term to the energy functional.

For  $\gamma \geq 1$ , the system eq. (2)–eq. (3) admits a unique global weak solution in an appropriate Sobolev space, given reasonable assumptions on the data; see [29, Proposition 6]. The proof deploys the convexity of the energy functional for  $\gamma \geq 1$ , allowing the application of Rockafellar's theorem. Currently, no known results establish well-posedness in Sobolev spaces for  $\gamma < 1$ . However, under stronger

regularity assumptions on the data, a local well-posedness result in Hölder spaces has been recently obtained [11]. For further details on the derivation and comprehensive analysis of the gradient flow structure in this model, we refer the reader to [26, 29, 30, 31, 46].

A key novelty of this work is the treatment of the energy cost functional without the commonly assumed linear diffusion term introduced via the Dirichlet integral, which has been extensively studied in the literature [10, 26, 27, 29]. This diffusion term accounts for random fluctuations in the medium, typically modeled as Brownian motion. Remarkably, even in the absence of linear diffusion, complex and rich network structures naturally emerge, driven by the positive feedback loop between the tensor-product term  $\nabla p \otimes \nabla p$  in eq. (3) and the flux  $(C+r\mathbb{I})\nabla p$  generated by the Poisson equation eq. (2). This highlights the fundamental role of the conductivity tensor in shaping emergent network patterns in biological systems. In contrast, for a vectorial model studied in [27], where the conductivity matrix is assumed to be of the form  $\mathbb{C} = \mathbf{m} \otimes \mathbf{m}$ , linear diffusion was crucial for the initial propagation of the material layers and, consequently, for the formation of network structures.

Various methods based on finite elements have been considered in the literature for the solution of the vectorial model, using Crank–Nicolson [3], semi-implicit first-order schemes [22, 28], and, more recently, sophisticated energy dissipation preserving schemes [33, 52]. Recent works [7, 9] have proposed semi-implicit solvers for the numerical solution of the differential-algebraic system of equations arising from similar constrained gradient-flow dynamics as eq. (3). Finite difference approximations in space with semi-implicit time discretizations using a symmetric alternating direction scheme have been proposed in [9], while a finite element discretization coupled with a semi-implicit backward Euler scheme has been proposed in [7]. Both works highlight the ill-conditioning of the problem when  $\gamma < 1$  and  $r \rightarrow 0$ . For such values of  $\gamma$ , the energy functional is not convex, and numerical errors, amplified by the ill-conditioning of the Poisson problem as  $r \rightarrow 0$ , accumulate over time and result in the appearance of spurious secondary branches in the final network structure. Also, the numerical results using a continuous bi-linear finite element-based discretization for the conductivity matrix exhibit oscillatory behavior of the energy as the steady state is approached [7].

In this work, we design a fully implicit nonlinear solution strategy using finite element discretizations that preserve the energy decay as time advances and the symmetries, if any, of the final network structure. Key to the success of our approach is the discretization of the conductivity matrix using discontinuous finite element spaces, which eases the preservation of its positive semi-definiteness. Equally important is the design of a robust and scalable preconditioning strategy with respect to the ill-conditioning of the Poisson problem. Together, these techniques enable the efficient and practical solution of the nonlinear systems arising from implicit time-stepping schemes. The entire algorithm is implemented in a distributed-memory framework, making it possible to simulate highly refined network structures at large scale and three-dimensional structures.

In [32], it has been shown that for  $\gamma < 1$ , every minimizer of the energy eq. (1) is an acyclic (i.e., loop-free) graph, and vice versa, every acyclic graph generates a local minimizer of the energy. For  $\gamma = 1$ , the minimizer is a set containing an acyclic graph. Therefore, assuming that the sequence of minimizers converges in the continuum limit, we do not expect the limiting structure to have any finite resolution

scale. This also means that any mesh refinement in the discretization of the problem eq. (2)–eq. (3) produces new, finer structures, with resolution corresponding to the length of the mesh elements, and that different meshes may generate different network structures. A robust solver can thus enable us to explore how different mesh resolutions and topologies influence emergent network structures.

For the first time, we provide three-dimensional numerical results of the system (2)–(3), marking a significant advancement in the field. Previous numerical studies, such as [4, 8, 28], were limited to lower-dimensional settings due to the prohibitive computational cost of simulating such processes in three dimensions. This breakthrough opens new possibilities for studying the formation of biological transportation networks in a realistic setting with unprecedented detail and accuracy.

The paper is structured as follows: section 2 introduces the model and the main assumptions. Section 3 details the finite element discretization, the choice of the time-advancing scheme, and the design of the nonlinear solution strategy. Numerical results are presented and discussed in section 4. Conclusions are drawn in section 5.

## 2. MODEL

The primary objective of this paper is to design robust solvers and to conduct several numerical experiments; as a first step, we introduce a parameter reduction through a suitable scaling of the energy functional eq. (1). Specifically, we consider the following rescaling

$$(4) \quad \begin{aligned} E_{c,\nu,\gamma}[\mathbb{C}] &= c^2 \int_{\Omega} \nabla p \cdot (\mathbb{C} + r\mathbb{I}) \nabla p + \frac{\nu}{c^2\gamma} \left( \|\mathbb{C}\|^2 + \varepsilon \right)^{\frac{\gamma}{2}} dx \\ &=: c^2 E_{\tilde{\nu},\gamma}[\mathbb{C}], \end{aligned}$$

where  $\tilde{\nu} = \frac{\nu}{c^2}$ . Furthermore, under this scaling, the natural time variable in the evolution of the system is  $\tilde{t} = c^2 t$ . From now on, we will drop the tilde superscript and use  $E$ ,  $t$ , and  $\nu$  for notational simplicity.

In this work, we thus focus on the numerical solution of the following differential-algebraic system:

$$(5) \quad \begin{cases} \frac{\partial \mathbb{C}}{\partial t} = \nabla p \otimes \nabla p - \nu \left( \|\mathbb{C}\|^2 + \varepsilon \right)^{\frac{\gamma-2}{2}} \mathbb{C} & \text{in } \Omega \times [0, \infty), \\ -\nabla \cdot ((\mathbb{C} + r\mathbb{I}) \nabla p) = S & \text{in } \Omega \times [0, \infty), \\ (\mathbb{C} + r\mathbb{I}) \nabla p \cdot \mathbf{n} = 0 & \text{in } \partial\Omega \times [0, \infty), \\ \mathbb{C}(x, t=0) = \mathbb{C}_0(x) \geq 0 & \text{in } \Omega, \end{cases}$$

where the positivity of the initial condition is understood in the sense of matrices, and  $\mathbf{n}$  denotes the outward-pointing unit normal vector to the boundary  $\partial\Omega$ . To ensure the solvability of the Poisson equation subject to the homogeneous Neumann boundary conditions, we impose the global balance of sources and sinks (in other words, global conservation of mass),

$$\int_{\Omega} S(x) dx = 0.$$

The model under consideration is derived as the  $L^2$ -gradient flow of eq. (4), subject to the elliptic constraint eq. (2) with no-flux boundary conditions. Its

derivation relies on well-established techniques as presented in [5, 41, 48], and the explicit computation in the biological network setting can be found in [26, 30, 46]. We note that we employ the gradient flow approach not only as a procedure to find (local) minima of the energy functional. Instead, we are interested in studying network formation as a dynamical process. Starting from a generic (and ‘simple’) initial datum, e.g.,  $\mathbb{C}_0(x) \equiv \mathbb{I}$  in  $\Omega$ , we follow the gradient flow dynamics to observe the self-organization of the network, creation, and refinement of branches, until a steady state is reached.

We note that, by virtue of the gradient flow structure, the energy functional  $E$  decreases along solutions  $\mathbb{C}$  of the system (see [41]). Moreover, the positive semi-definiteness of  $\mathbb{C}$  is preserved along the flow; to prove this, fix an arbitrary vector  $\xi \in \mathbb{R}^d$  and define  $z(x, t) := \xi \cdot \mathbb{C}(x, t) \xi$ . Multiplying eq. (3) by  $\xi$  on both sides yields

$$\frac{\partial z}{\partial t} = |\nabla p \cdot \xi|^2 - \nu \left( \|\mathbb{C}\|^2 + \varepsilon \right)^{\frac{\gamma-2}{2}} z \geq -\nu \left( \|\mathbb{C}\|^2 + \varepsilon \right)^{\frac{\gamma-2}{2}} z,$$

with initial condition  $z(x, 0) = z_0(x) := \xi \cdot \mathbb{C}_0(x) \xi \geq 0$ . By applying a Grönwall-type argument, we deduce that

$$z \geq z_0 \exp \left( -\nu \int_0^t \left( \|\mathbb{C}(x, s)\|^2 + \varepsilon \right)^{\frac{\gamma-2}{2}} ds \right) \geq 0.$$

Hence,  $\mathbb{C}$  remains positive semi-definite for all  $t \geq 0$  and  $x \in \Omega$ .

### 3. NUMERICAL SCHEME

**3.1. Semi-discrete formulation.** We base the numerical scheme on the Finite Element Method (FEM, [19]). We thus proceed in a standard way and introduce the variational formulation of eq. (3), working with the Sobolev spaces

$$\mathbf{C} = \left\{ \mathbb{B} \in [L^2(\Omega)]^{d \times d} : \mathbb{B} = \mathbb{B}^T \right\}, \quad P = \left\{ q \in H^1(\Omega) : \int_{\Omega} q = 0 \right\}.$$

Multiplying by test functions  $(\mathbb{B}, q)$ , integrating over the domain, and by using integration by parts (taking into account the natural boundary conditions on  $\mathbb{C}$ ), we obtain

$$\begin{aligned} \int_{\Omega} (\mathbb{C} + r\mathbb{I}) \nabla p \cdot \nabla q \, dx &= \int_{\Omega} Sq \, dx, & \forall q \in P, \\ \int_{\Omega} \left( \frac{\partial \mathbb{C}}{\partial t} : \mathbb{B} - (\nabla p \otimes \nabla p) : \mathbb{B} + \nu(\|\mathbb{C}\|^2 + \varepsilon)^{(\gamma-2)/2} \mathbb{C} : \mathbb{B} \right) \, dx &= 0, & \forall \mathbb{B} \in \mathbf{C}, \end{aligned}$$

which consists of  $d(d+1)/2$  equations for the components of the symmetric conductivity matrix and one equation for the pressure. We note that  $(\mathbb{C} + r\mathbb{I}) \nabla p$  is the usual matrix-vector product, while products of the form  $\mathbb{C} : \mathbb{B}$  should be understood entry-wise.

Introducing a tessellation  $\Omega_h \subset \Omega$  with a given mesh size  $h$  and the finite-dimensional subspaces

$$\mathbf{C}_h = \left\{ \mathbb{C}_h \in \mathbf{C} \mid \mathbb{C}_h = \sum_{j=1}^{N_c} a_j \Phi_j \right\}, \quad P_h = \left\{ p_h \in P \mid p_h = \sum_{j=1}^{N_p} a_j \varphi_j \right\},$$

we arrive at a semi-discrete formulation: Given  $S \in L^2(\Omega_h)$ , find  $p_h \in P_h$  and  $\mathbb{C}_h \in \mathbf{C}_h$  such that it holds

$$\begin{aligned} \int_{\Omega} (\mathbb{C}_h + r\mathbb{I}) \nabla p_h \cdot \nabla q_h \, dx &= \int_{\Omega} S q_h \, dx, & \forall q_h \in P_h, \\ \int_{\Omega} \left( \frac{\partial \mathbb{C}_h}{\partial t} : \mathbb{B}_h - (\nabla p_h \otimes \nabla p_h) : \mathbb{B}_h + \nu(\|\mathbb{C}_h\|^2 + \varepsilon)^{(\gamma-2)/2} \mathbb{C}_h : \mathbb{B}_h \right) dx &= 0, & \forall \mathbb{B}_h \in \mathbf{C}_h, \end{aligned}$$

which leads to a set of Differential-Algebraic equations (DAE)

$$\begin{aligned} (6) \quad \int_{\Omega} (\mathbb{C}_h + r\mathbb{I}) \nabla p_h \cdot \nabla \psi_i \, dx &= \int_{\Omega} S \psi_i \, dx, & \forall i \in 1, \dots, N_p, \\ \int_{\Omega} \left( \frac{\partial \mathbb{C}_h}{\partial t} : \Psi_i - (\nabla p_h \otimes \nabla p_h) : \Psi_i + \nu(\|\mathbb{C}_h\|^2 + \varepsilon)^{(\gamma-2)/2} \mathbb{C}_h : \Psi_i \right) dx &= 0, & \forall i \in 1, \dots, N_c, \end{aligned}$$

where  $\psi_i$  (resp.  $\Psi_i$ ) are test functions for  $P_h$  (resp.  $\mathbf{C}_h$ ).

In this work, we use finite element spaces consisting of piecewise constant polynomials for each component of the conductivity matrix and linear polynomials for the pressure space, i.e.,

$$\begin{aligned} \mathbf{C}_h &= \{ \mathbb{C}_h \in \mathbf{C} \mid \mathbb{C}_{h|K} \text{ constant, } \forall K \in \Omega_h \}, \\ P_h &= \{ \mathbb{P}_h \in P \mid \mathbb{P}_h \in C^0(\Omega_h) \text{ and } \mathbb{P}_{h|K} \text{ linear, } \forall K \in \Omega_h \}, \end{aligned}$$

where  $K$  is a cell of the tessellated domain  $\Omega_h$ . In the above definition for  $P_h$ , the term linear indicates bi-linear or tri-linear elements in case  $K$  is a tensor-product cell.

In two dimensions, we discretize the symmetric conductivity matrix with a three-component FEM space

$$\mathbb{C}_h = \begin{bmatrix} \mathbb{C}_h^0 & \mathbb{C}_h^1 \\ \mathbb{C}_h^1 & \mathbb{C}_h^2 \end{bmatrix},$$

using the same scalar basis for each component. The conductivity equations of eq. (6) can thus be rewritten

$$\begin{aligned} \int_{\Omega} \left( \frac{\partial \mathbb{C}_h^0}{\partial t} \Psi_i^0 - \frac{\partial p_h}{\partial x} \frac{\partial p_h}{\partial x} \Psi_i^0 + \nu(\|\mathbb{C}_h\|^2 + \varepsilon)^{(\gamma-2)/2} \mathbb{C}_h^0 \Psi_i^0 \right) dx &= 0, \\ \int_{\Omega} \left( \frac{\partial \mathbb{C}_h^1}{\partial t} \Psi_i^1 - \frac{\partial p_h}{\partial x} \frac{\partial p_h}{\partial y} \Psi_i^1 + \nu(\|\mathbb{C}_h\|^2 + \varepsilon)^{(\gamma-2)/2} \mathbb{C}_h^1 \Psi_i^1 \right) dx &= 0, \\ \int_{\Omega} \left( \frac{\partial \mathbb{C}_h^2}{\partial t} \Psi_i^2 - \frac{\partial p_h}{\partial y} \frac{\partial p_h}{\partial y} \Psi_i^2 + \nu(\|\mathbb{C}_h\|^2 + \varepsilon)^{(\gamma-2)/2} \mathbb{C}_h^2 \Psi_i^2 \right) dx &= 0, \end{aligned}$$

where we have used the same split for the trial functions

$$\Psi_i = \begin{bmatrix} \Psi_i^0 & \Psi_i^1 \\ \Psi_i^1 & \Psi_i^2 \end{bmatrix}.$$

For symmetry reasons (see section 3.3 for details), we further rescale the above equations and the pressure equation of eq. (6) as

$$(7) \quad \begin{aligned} - \int_{\Omega} (\mathbb{C}_h + r\mathbb{I}) \nabla p_h \cdot \nabla q_h \, dx &= - \int_{\Omega} S q_h \, dx, \\ \frac{1}{2} \int_{\Omega} \left( \frac{\partial \mathbb{C}_h^0}{\partial t} \Psi_i^0 - \frac{\partial p_h}{\partial x} \frac{\partial p_h}{\partial x} \Psi_i^0 + \nu(\|\mathbb{C}_h\|^2 + \varepsilon)^{(\gamma-2)/2} \mathbb{C}_h^0 \Psi_i^0 \right) dx &= 0, \\ \int_{\Omega} \left( \frac{\partial \mathbb{C}_h^1}{\partial t} \Psi_i^1 - \frac{\partial p_h}{\partial x} \frac{\partial p_h}{\partial y} \Psi_i^1 + \nu(\|\mathbb{C}_h\|^2 + \varepsilon)^{(\gamma-2)/2} \mathbb{C}_h^1 \Psi_i^1 \right) dx &= 0, \\ \frac{1}{2} \int_{\Omega} \left( \frac{\partial \mathbb{C}_h^2}{\partial t} \Psi_i^2 - \frac{\partial p_h}{\partial y} \frac{\partial p_h}{\partial y} \Psi_i^2 + \nu(\|\mathbb{C}_h\|^2 + \varepsilon)^{(\gamma-2)/2} \mathbb{C}_h^2 \Psi_i^2 \right) dx &= 0, \end{aligned}$$

Similar arguments hold for the three-dimensional case and are omitted.

**3.2. Time discretization.** We now discuss the selection of a suitable time integration scheme. To this end, we first observe that the semi-explicit index-1 DAE in eq. (6) forms a compact set of nonlinear equations of the type [6]

$$(8) \quad F(\dot{\mathbf{u}}, \mathbf{u}, t) = 0,$$

where we have used  $\mathbf{u}$  to denote the vector of degrees of freedom, ordered by fields, associated with the finite element functions  $\mathbb{C}_h$  and  $p_h$ ; for example, in two dimensions,

$$\mathbf{u} = \begin{bmatrix} \mathbb{C}_h^0 \\ \mathbb{C}_h^1 \\ \mathbb{C}_h^2 \\ p_h \end{bmatrix},$$

where with abuse of notation, we used the finite element function to denote the vector of associated degrees of freedom. Specific to the choice of the time integrator is the approximation of the time derivative vector  $\dot{\mathbf{u}}$ ; in particular, using the backward Euler (BE) method as the time integrator leads to the solution of the set of nonlinear equations

$$(9) \quad F \left( \frac{\mathbf{u}_{n+1} - \mathbf{u}_n}{\delta t_n}, \mathbf{u}_{n+1}, t_n + \delta t_n \right) = 0,$$

where  $\mathbf{u}_n$  denotes the known solution at the  $n$ -th time step,  $t_n$  is the current time,  $\delta t_n$  is the current time step, and  $\mathbf{u}_{n+1}$  is the vector of unknowns for the solution at the  $n+1$ -th step.

In our case, the energy functional eq. (4) is convex if and only if  $\gamma \geq 1$ ; in such cases, the backward Euler scheme will guarantee convergence to a global minimum and will maintain the energy decay property (note that  $\lambda$ -convexity is enough if  $\delta t$  is sufficiently small). However, if the convexity of  $E$  is dropped, then the existence and uniqueness of the solution  $\mathbf{u}_{n+1}$  is questionable, as it is its energy decay. It is well established that the backward Euler scheme is unconditionally stable, meaning it converges to a stationary point regardless of the chosen time step. Nevertheless, it does not necessarily preserve the structural properties of the system. For a detailed discussion on the convergence of BE to equilibrium, we refer to [20, 40]. Conversely, the explicit Euler method ensures dissipation but often requires very restrictive conditions on the time step in relation to the spatial discretization. We further note here that when the energy functional satisfies suitable smoothness, coercivity, and convexity conditions, discrete gradient methods provide unconditional stability

and ensure a monotone decrease of the energy throughout the iterations (see, e.g., [25]).

Considering the solution of the DAE system, using the backward Euler method will lead to a time-advancing scheme of the first order. For higher-order time integrations of DAEs, a popular choice is the so-called BDF method based on backward differential formulas for the approximation of the time-derivative vector [24]

$$(10) \quad F \left( \sum_{k=0}^s \alpha_k \mathbf{u}_{n+1-k}, \mathbf{u}_{n+1}, t_n + \delta t_n \right) = 0,$$

where the coefficients  $\alpha_k$  are chosen using Lagrangian interpolation polynomials to achieve a global  $s$ -order convergence for the method. For  $k = 1$ , we recover the backward Euler scheme eq. (9). Another popular second-order method is the Crank–Nicolson method, which uses a trapezoidal rule to evaluate the right-hand side of explicit ordinary differential equations

$$(11) \quad \mathbf{u}_{n+1} = \mathbf{u}_n + \frac{\delta t_n}{2} [f(\mathbf{u}_n) + f(\mathbf{u}_{n+1})],$$

where the equation is expressed in the explicit form  $\dot{\mathbf{u}} = f(\mathbf{u}, t)$ .

It is straightforward to prove that the backward Euler scheme preserves the positive semi-definiteness of the conductivity matrix. To this end, we first rewrite the equations for  $\mathbb{C}$  eq. (3) as

$$\frac{\partial \mathbb{C}}{\partial t} = \mathbb{G}(p) - m(\mathbb{C})\mathbb{C}, \quad \mathbb{G}(p) = \nabla p \otimes \nabla p, \quad m(\mathbb{C}) = \nu \left( \|\mathbb{C}\|^2 + \varepsilon \right)^{\frac{\gamma-2}{2}},$$

and note that  $\mathbb{G}(p)$  is a SPSD matrix and  $m(\mathbb{C}) > 0$ . The BE equations eq. (9) arising from eq. (6) can be rewritten as

$$\int_{\Omega} \left[ (1 + m(\mathbb{C}_{n+1})\delta t) \mathbb{C}_{n+1} : \Psi_i \right] dx = \int_{\Omega} \left[ (\mathbb{C}_n + \mathbb{G}(p_{n+1})\delta t) : \Psi_i \right] dx.$$

Thus, if  $\mathbb{C}_n$  is SPSD,  $\mathbb{C}_{n+1}$  will also be SPSD since  $1 + m(\mathbb{C}_{n+1})\delta t > 0$ ,  $\Psi_i$  are positive piecewise constant test functions, and the right-hand side consists of the weighted sum of SPSD matrices sampled at the quadrature nodes used by the FEM method. Nevertheless, at the numerical level, we need to solve the above equations very accurately if we want to guarantee the positive semi-definiteness of the conductivity matrix. In addition, care must be exercised when using higher-order polynomials to discretize the conductivity matrix. To ensure the positivity of the basis at the quadrature nodes, one may use, for instance, the Bernstein polynomials [37]. We stress that the discontinuity of the discretization space is crucial to prove the positive semi-definiteness of  $\mathbb{C}_{n+1}$ . The use of a  $H^1(\Omega)$  conforming space, as needed in the presence of the diffusion term for  $\mathbb{C}$  in the energy functional, will require the finite element spaces to guarantee the preservation of the maximum principle, a condition very hard to realize in practice; see, e.g., [23] and the references therein.

The positive semi-definiteness of  $\mathbb{C}$  is generally not preserved by the BDF or CN methods. For example, for BDF of order 2 (similar arguments hold for higher-order

formulas), the equations arising from eq. (10) are

$$\int_{\Omega} \left[ (1 + m(\mathbb{C}_{n+1})\delta t) \mathbb{C}_{n+1} : \Psi_i \right] dx = \int_{\Omega} \left[ \left( \frac{4}{3} \mathbb{C}_n - \frac{1}{3} \mathbb{C}_{n-1} + \mathbb{G}(p_{n+1})\delta t \right) : \Psi_i \right] dx,$$

where, without loss of generality, we have assumed constant time steps. In this case, we cannot guarantee the positive semi-definiteness of  $\mathbb{C}_{n+1}$  since the  $\mathbb{C}_{n-1}$  term contributes a negative shift by an SPD matrix. Similar arguments hold for the CN update

$$\int_{\Omega} \left[ \left( 1 + \frac{\delta t}{2} m(\mathbb{C}_{n+1}) \right) \mathbb{C}_{n+1} : \Psi_i \right] dx = \int_{\Omega} \left[ \left( \mathbb{C}_n + \frac{\delta t}{2} [\mathbb{G}(p_n) + \mathbb{G}(p_{n+1}) - m(\mathbb{C}_n)\mathbb{C}_n] \right) : \Psi_i \right] dx,$$

where now the SPD term  $m(\mathbb{C}_n)\mathbb{C}_n$  contributes a negative shift to the update.

We close this Section with a final note on the use of operator-splitting techniques. They can still be applied in this context, and we can obtain the ones considered in [7, 9] by just sampling  $\nabla p_h \otimes \nabla p_h$  and  $(\|\mathbb{C}_h\|^2 + \varepsilon)^{(\gamma-2)/2}$  appearing in eq. (6) with values coming from the previous time step. Similar observations for the preservation of the positive semi-definiteness of the conductivity matrix can be drawn.

**3.3. Nonlinear solver.** Once the time integrator is set, at each time step of the simulation, we solve the associated nonlinear equations

$$G(\mathbf{u}^*) = 0,$$

using the inexact Newton's method [44]; starting from an initial iterate  $\mathbf{u}_0^*$ , usually the solution of the previous time-step, we compute successive approximations of the solution through the linear approximation

$$\mathbf{u}_{k+1}^* = \mathbf{u}_k^* - \lambda_k J(\mathbf{u}_k^*)^{-1} G(\mathbf{u}_k^*)$$

where  $J(\mathbf{u}_k^*)$  is the Jacobian of  $G$  evaluated at the current linearization point  $\mathbf{u}_k^*$ , and  $\lambda_k$  is selected with a line-search strategy. The Jacobian of  $G$  can be obtained by considering the generalized Jacobian of eq. (8)

$$(12) \quad J = \sigma \frac{\partial F}{\partial \dot{\mathbf{u}}} + \frac{\partial F}{\partial \mathbf{u}}$$

where  $\sigma$  is a scalar associated with the current time step choice [6]. For example, for BE,  $\sigma = 1/\delta t_n$ .

We are interested in very fine discretizations, and we thus need to resort to Krylov methods for the approximate solution of the Jacobian linear system. Since the choice of the preconditioner is crucial for the convergence of such methods, here we explicitly write the Jacobians for the two-dimensional case, using the symmetrized residual equations eq. (7); similar arguments hold for the three-dimensional case, but we omit the redundant details. To clarify the notation, we use  $\phi_j$  for the scalar components of the conductivity fields and  $\varphi_j$  for the pressure.

The Jacobian of the time-dependent part of eq. (12) is independent of the linearization point, and it is given by

$$\frac{\partial F}{\partial \dot{\mathbf{u}}} = \begin{bmatrix} \frac{1}{2}M & 0 & 0 & 0 \\ 0 & M & 0 & 0 \\ 0 & 0 & \frac{1}{2}M & 0 \\ 0 & 0 & 0 & 0 \end{bmatrix},$$

where  $M$  is the mass matrix associated with the basis of the conductivity components

$$M_{ij} = \int_{\Omega} \phi_i \phi_j dx.$$

The Jacobian of the time-independent part of eq. (12) is instead a block matrix with structure

$$\frac{\partial F}{\partial \mathbf{u}} = \begin{bmatrix} A^{00} & 2A^{01} & A^{02} & B^0 \\ 2A^{10} & 4A^{11} & 2A^{12} & B^1 \\ A^{20} & 2A^{21} & A^{22} & B^2 \\ B^{0T} & B^{1T} & B^{2T} & -D \end{bmatrix},$$

where

$$\begin{aligned} A_{ij}^{mn} &= \nu \int_{\Omega} (\alpha + \beta \mathbb{C}_h^m \mathbb{C}_h^n) \phi_i \phi_j dx, \quad m, n = 0, 1, 2 \\ B_{ij}^0 &= - \int_{\Omega} \phi_i \frac{\partial p_h}{\partial x} \frac{\partial \varphi_j}{\partial x} dx, \\ B_{ij}^1 &= - \int_{\Omega} \phi_i \left( \frac{\partial p_h}{\partial y} \frac{\partial \varphi_j}{\partial x} + \frac{\partial p_h}{\partial x} \frac{\partial \varphi_j}{\partial y} \right) dx, \\ B_{ij}^2 &= - \int_{\Omega} \phi_i \frac{\partial p_h}{\partial y} \frac{\partial \varphi_j}{\partial y} dx, \\ D_{ij} &= \int_{\Omega} (\mathbb{C}_h + r\mathbb{I}) \nabla \varphi_i \cdot \nabla \varphi_j dx, \end{aligned}$$

and with coefficients

$$(13) \quad \alpha = (\|\mathbb{C}_h\|^2 + \varepsilon)^{(\gamma-2)/2}, \quad \beta = \frac{\gamma-2}{2} (\|\mathbb{C}_h\|^2 + \varepsilon)^{(\gamma-4)/2}.$$

Grouping the conductivity blocks, we can write the symmetric indefinite Jacobian matrix eq. (12) as

$$J = \begin{bmatrix} J_{00} & J_{01} \\ J_{01}^T & -D \end{bmatrix}.$$

A discontinuous discretization space for  $\mathbb{C}$  leads to a trivially invertible  $J_{00}$  block since the latter is a block diagonal matrix with a 3x3 sub-block for each cell; we can thus consider an exact Schur complement factorization of  $J$  as

$$(14) \quad \begin{bmatrix} J_{00} & J_{01} \\ J_{01}^T & -D \end{bmatrix} = \begin{bmatrix} J_{00} & 0 \\ J_{01}^T & I \end{bmatrix} \begin{bmatrix} J_{00}^{-1} & 0 \\ 0 & -S \end{bmatrix} \begin{bmatrix} J_{00} & J_{01} \\ 0 & I \end{bmatrix}, \quad S = D + J_{01}^T J_{00}^{-1} J_{01},$$

that requires solving the inexpensive block-diagonal problem  $J_{00}$  twice, and the Schur complement system  $S$  only once. Note that the Schur complement  $S$  is a symmetric positive semi-definite matrix representing a perturbed scalar diffusion problem since  $J_{00}$  is a symmetric positive definite (SPD) matrix,  $M$  is SPD, each  $A^{mn}$  block is SPD, and  $A^{mn} = A^{nm}$ . The semi-definiteness of  $S$  is due to the fact that the kernel of the column spaces of  $D$  and  $J_{01}$  contain the constant.

In the implementation, the exact inverse of the Schur complement  $S$  can be replaced with the action of a nested Krylov method, and the above factorization can be used as a preconditioner within any outer Krylov method designed for indefinite systems. Alternatively, we can also consider the block-diagonal, positive semi-definite approximation

$$\begin{bmatrix} J_{00} & 0 \\ 0 & S \end{bmatrix},$$

within a MINRES algorithm [42, 45].

Given the fact that the Schur complement matrix can be inexpensively constructed, an optimal choice for preconditioning the Schur complement is thus an algebraic multigrid (AMG) preconditioner, which guarantees robustness and has an overall cost that is linear in the matrix size [51]; in alternative, non-overlapping domain decomposition methods like the Balancing Domain Decomposition by Constraints preconditioner [53] can also be considered given the considerable heterogeneity of the conductivity matrix within the domain.

#### 4. NUMERICAL EXPERIMENTS

The code used to conduct the numerical experiments described in this Section is public<sup>1</sup>. It is based on the Portable and Extensible Toolkit for Scientific Computing (PETSc), a software library specifically designed to solve large-scale nonlinear systems of equations arising from partial differential equations in a distributed memory fashion using the Message Passing Interface (MPI) [12, 13, 14]. Numerical simulations are performed using the Shaheen III supercomputer at KAUST, an HPE Cray EX system with 4608 AMD-powered compute nodes tightly connected with a low-latency/high-speed Slingshot network. Each compute node is a dual-socket AMD EPYC 9654 of the Genoa family, with 192 cores per node and 384GB of DDR5 memory. Instructions to run the code and reproduce the results shown in this Section are available at [54].

The management of unstructured grids and the implementation of FEM are based on the DMPLEX infrastructure [38, 39], which facilitates the writing of dimension-independent kernels while supporting both simplicial and tensor-product cells. Time integration is performed using the TS module [1], which allows a seamless switch between DAE integrators for experimentation purposes; adaptive time stepping is performed using digital filtering-based methods [49] combined with the evaluation of the local truncation error using extrapolation techniques. Unless otherwise stated, the nonlinear systems of equations arising from the time-advancing schemes are solved with a tight absolute tolerance of 1.E-14; Jacobian linear systems are solved using the right-preconditioned GMRES method [47] with the Schur complement-based preconditioner given in eq. (14), where the Schur complement solver is replaced by the application of an AMG preconditioner based on smoothed aggregation [2]. Linear system tolerances are dynamically adjusted using the well-known Eisenstat and Walker trick, which prevents over-solving in the early steps of the Newton process and tightens the accuracy as convergence is approached [21]. The usual cubic backtracking algorithm is used for the line search.

**4.1. Scalability.** We first report on the parallel scalability of the main components of the solver, namely the evaluation of the nonlinear residual  $F$  eq. (8) and the Jacobian  $J$  eq. (12), together with the setup and application timings of the Schur complement-based preconditioner eq. (14). For this test, we run the backward Euler solver for five time steps and collect average timings in fig. 2. In the left panel, we report the timings of a strong scaling test. The mesh is fixed and obtained with three uniform refinements of the leaf mesh<sup>2</sup> shown in fig. 1, which has been obtained using the ngsPETSc package [17]. The number of MPI processes (subdomains) is

<sup>1</sup>Available at <https://gitlab.com/petsc/petsc/-/blob/main/src/ts/tutorials/ex30.c>

<sup>2</sup>Available at <https://gitlab.com/petsc/datafiles/-/blob/main/meshes/leaf.h5>

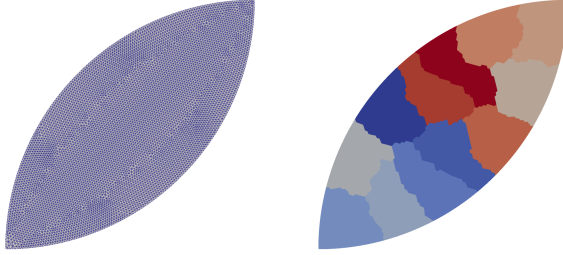


FIGURE 1. Left: leaf mesh, right: example decomposition with 12 subdomains.

increased from 1 to 192; the number of degrees of freedom (dofs) for the strong scaling test is 2.9 million. In the right panel, we instead report the timings of a weak scaling setup, where both the number of cells in the mesh and the number of MPI processes are proportionally increased, with the number of dofs ranging from 2.9 million to 186.5 million, while the number of processes goes from 192 to 12288, thus keeping fixed the workload per process at about 15 thousand dofs. All solver components scale almost ideally in the range of processes considered.

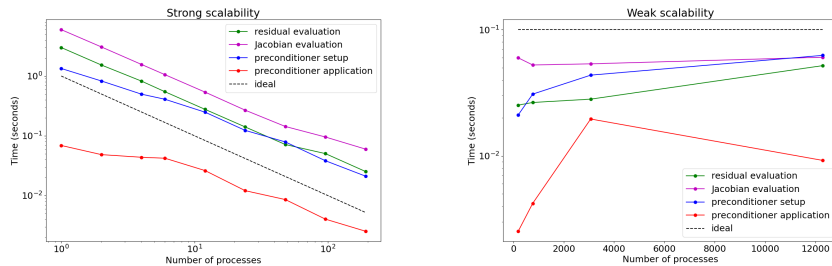


FIGURE 2. Parallel scalability: strong scaling (left) and weak scaling (right) results compared against the ideal case. See section 4.1 for additional details.

**4.2. Network formation.** Here, we report on the network formation process using the backward Euler-based nonlinear solver. For this experiment, we fix the model parameters to  $\varepsilon = 1.E-5$ ,  $r = 1.E-4$ ,  $\gamma = 0.75$ , and  $\nu = 0.03$ . The domain is the unit square  $\Omega = [0, 1]^2$ , discretized with a structured quadrilateral mesh with a 1024x1024 cell arrangement; the total number of dofs is 4.2 million. The initial conductivity matrix  $\mathbb{C}_0 = \mathbb{C}_0(x)$  is chosen to be the constant identity matrix in  $\Omega$ . The simulations are run up to time 200, and we use the Gaussian source

$$(15) \quad S(x) = S_0(x) - \int_{\Omega} S_0(x) \, dx, \quad S_0(x) = e^{-500\|x-x_0\|^2},$$

with  $x_0 = (0.25, 0.25)$ .

fig. 3 shows the energy of the system  $E$  (left panel), the negative time derivative of the energy  $-\frac{\partial E}{\partial t}$  (central panel), and the time step taken  $\delta t$  (right) by the solver in a semi-logarithmic scale as a function of the simulated time. In fig. 4, we report

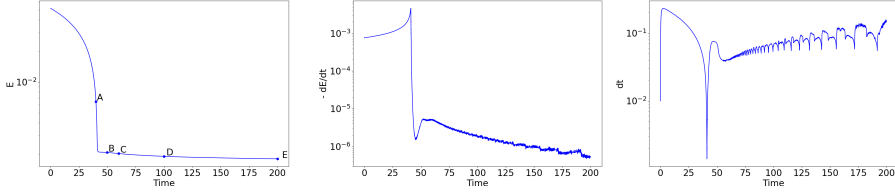


FIGURE 3. Energy (left panel),  $-\frac{\partial E}{\partial t}$  (center), and time step (right), as a function of simulation time for 1024x1024 mesh. See section 4.2 for additional details.

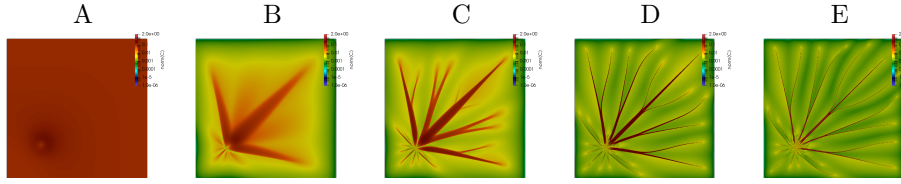


FIGURE 4.  $\|\mathbb{C}\|$  at selected time instances (see fig. 3) for 1024x1024 mesh in logarithmic scale. See section 4.2 for additional details.

snapshots of  $\|\mathbb{C}\|$  at selected time instances as indicated in the text boxes in fig. 3; these plots are given in logarithmic scale to appreciate the network ramifications fully.

The system's energy is monotonically decreasing; we observe a rapid decay in the early phases of the simulation, where the norm of the conductivity matrix is propagating almost homogeneously within the domain (see panel A in fig. 4), and relatively large time steps can be taken. During the early stage, a smooth pattern in  $\mathbb{C}$  is formed due to the positive tensor-product term  $\nabla p \otimes \nabla p$  in eq. (3) and the energy variations are associated with the  $\nabla p \cdot (\mathbb{C} + r\mathbb{I})\nabla p$  term. After this initial phase, the network begins to form (see panels B and C in fig. 4) due to the interplay of the positive tensor product term and the negative term  $-\nu (\|\mathbb{C}\|^2 + \varepsilon)^{\frac{\gamma-2}{2}} \mathbb{C}$ ; energy variations are smaller, and the time step automatically selected by the solver is also decreased. In the final part of the simulation, the energy continues to decrease toward its steady state at a slower pace with minimal variations to the conductivity matrix (see panels D and E in fig. 4), and relatively larger time steps can be taken. The network patterns at all time instances are symmetric along the bisector of the domain, confirming the robustness of the fully implicit solver.

**4.3. Robustness with respect to the mesh size.** In the next set of experiments, we study the robustness of the backward Euler solver with respect to the mesh size. For these experiments, we use the same model parameters as in section 4.2 and consider three levels of refinements of a structured quadrilateral mesh; the number of cells is 1024x1024, 2048x2048, and 4096x4096, and the corresponding number of dofs is 4.2, 16.8, and 67.1 million respectively. For these results, we keep the size of the local meshes approximately constant and use an increasing number of MPI processes: 384, 1536, and 6144. fig. 5 shows the energy of the system  $E$  (upper left panel), the negative time derivative of the energy  $-\frac{\partial E}{\partial t}$  (central panel), and the

time step taken  $\delta t$  by the solver (right) in a semi-logarithmic scale as a function of the simulated time. The final states of  $\|\mathbb{C}\|$  in logarithmic scale are shown in fig. 6.

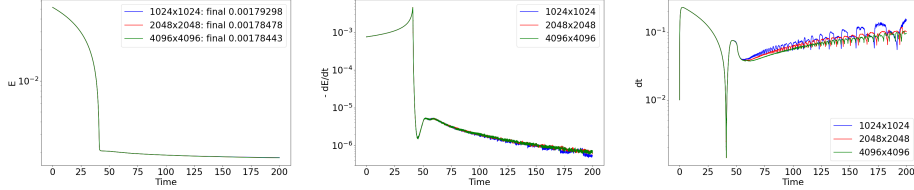


FIGURE 5. Energy (left panel),  $-\frac{\partial E}{\partial t}$  (center), and time step (right), as a function of simulation time for 1024x1024 (blue), 2048x2048 (red), and 4096x4096 (green) meshes. See section 4.3 for additional details.

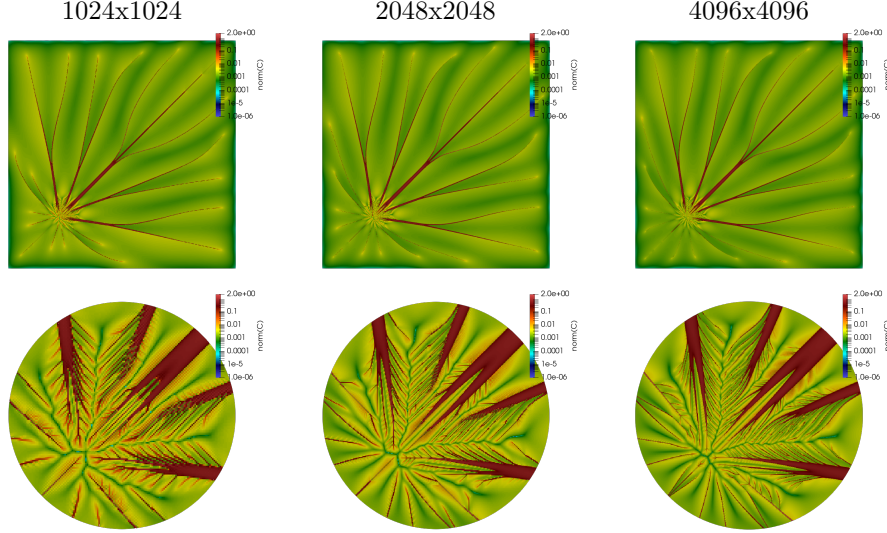


FIGURE 6. Final state of  $\|\mathbb{C}\|$  for 1024x1024 (left), 2048x2048 (center), and 4096x4096 (right) meshes. Bottom row: close-ups at the source location. See section 4.3 for additional details.

The network is well resolved away from the source location for all three resolutions; the robustness of the fully nonlinear solver is evident here since the network patterns are all symmetric along the bisector of the domain. Zooming on the source location (see fig. 6, bottom row), we can observe a checkerboard pattern for  $\|\mathbb{C}\|$  for the coarser mesh that naturally arises due to our choice of a discontinuous space for the conductivity matrix. Such a checkerboard pattern gets resolved as the mesh size decreases and finer structures are formed. We believe that for  $\gamma \leq 1$ , the analytical steady states (i.e., local minimizers of the energy eq. (1)) do not possess any definite scale. Therefore, any mesh refinement leads to the appearance of new, finer structures in the solution of the discretized problem, as can be observed in

fig. 6. From this point of view, the numerical results reflect the choice of the mesh used to solve the discretized problem. Different meshes would have led to different network structures, as demonstrated in section 4.6.

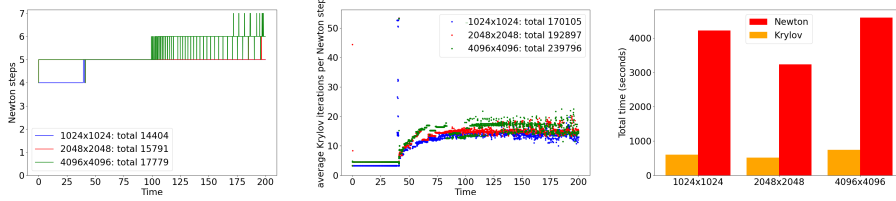


FIGURE 7. Newton steps (left panel), average number of linear iterations per Newton step (center), and timings (right) for BE solver and 1024x1024, 2048x2048, and 4096x4096 meshes. See section 4.3 for additional details.

We report the number of linear (central panel) and nonlinear (left) iterations of the three simulations, together with the time taken by the solver for the solution of the linear systems and the entire Newton solver (right) in fig. 5. The nonlinearity of the problem is not severe, and the total number of iterations is almost independent of the resolution, with the number of nonlinear iterations per time step between 4 and 7. The robustness of the Schur complement-based preconditioner is confirmed by the results shown in the central panel, where the average number of linear iterations is independent of the time step and almost always below 30 with a few outliers; linear systems are easy to solve in the early stages, while more iterations are needed as the network formation process progresses. The efficiency of the preconditioning step is also confirmed by the computational timings shown in the right panel. Total times are basically constant, proportional to the work per process, with the linear solver taking only a small fraction (below 20%) of the overall nonlinear solving time.

**4.4. Comparison with other time integrators.** Here, we analyze the preservation of the structure of the PDE when using second-order time integrators, namely Crank–Nicolson (CN) and BDF2. We consider the same model parameters as in section 4.3 and the finest 4096x4096 mesh. All solvers converge to a similar final energy value (see left panel of fig. 8), with all being able to preserve the energy decay (central panel). While CN and BDF2 allow for larger time steps (data not shown), neither can maintain the positive semi-definiteness of  $\mathbb{C}$  (see section 3.2); to quantify these errors, we compute

$$\frac{1}{|\Omega|} \int_{\Omega} \mathbb{1}_{\lambda_{min}(\mathbb{C}) < 0}(x) dx,$$

where  $\mathbb{1}_{(\cdot)}$  is the indicator function and  $\lambda_{min}(\mathbb{C})$  is the minimum eigenvalue of  $\mathbb{C}$ , sampled at the quadrature points of the FEM discretization. As expected, BE never computes solutions that lead to negative eigenvalues of  $\mathbb{C}$ , while BDF2 and CN fail, with BDF2 failing to preserve positive semi-definiteness even in 10% of the domain. The absolute values of the negative eigenvalues encountered by BDF2 or CN are nevertheless very small in this case and always below  $r$  (data not shown). We stress here that, at every evaluation of the residual equations eq. (6), we ensure

the Poisson problem is always well posed by sampling  $\mathbb{C} + r\mathbb{I}$  at the quadrature nodes, and by shrinking the time step if we encounter any negative eigenvalue. In fig. 9, we show the final state for  $\|\mathbb{C}\|$  for the three solvers considered, all of which preserve the symmetry of the solution.

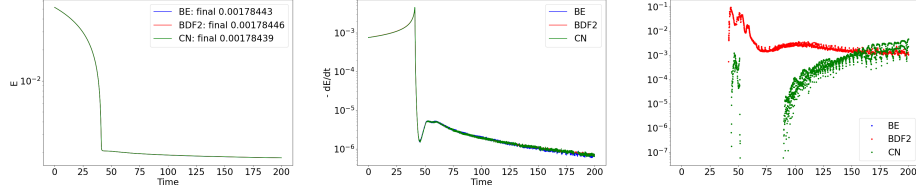


FIGURE 8. Energy (left panel),  $-\frac{\partial E}{\partial t}$  (center), and  $\frac{1}{|\Omega|} \int_{\Omega} \mathbf{1}_{\lambda_{\min}(\mathbb{C}) < 0} dx$  as a function of simulation time for Crank–Nicolson (CN, green), BDF2 (red) and BE (blue). See section 4.4 for additional details.

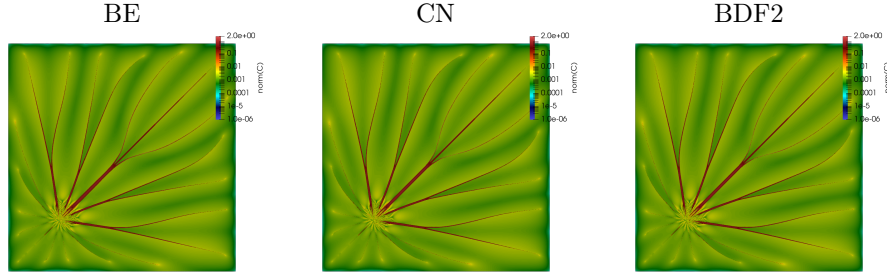


FIGURE 9. Final state of  $\|\mathbb{C}\|$  for BE (left column), CN (center), and BDF2 (right). See section 4.3 for additional details.

**4.5. Robustness against Poisson regularization  $r$ .** Here, we numerically demonstrate the robustness of the linear solver with respect to the regularization parameter  $r$ . When using semi-implicit methods for time advancing, we need to solve a Poisson problem where the size of the near-nullspace grows as  $r$  and  $\|\mathbb{C}\|$  approach zero, thus worsening the numerical stability of the algebraic solver. On the other hand, we do not solve the Poisson problem within the Newton process; instead, we solve a regularized version of it with a mass-dominated regularization within the Schur-complement preconditioning step (see section 3.3 for details). We thus expect that the number of linear iterations will not be significantly affected by  $r$ .

To validate such intuition, we use the 1024x1024 mesh and run different backward Euler-based simulations with the same model parameters as before but with different values of  $r$ . We report the results in fig. 10. The average number of linear iterations per step decreases as  $r$  decreases, and the total number of linear iterations is independent of  $r$  (see the central panel of fig. 10). The computational times for the Krylov solver are also independent of  $r$ . Still, those associated with the overall Newton solver increase as  $r$  decreases (right panel) since smaller values of

$r$  lead to more steps needed to converge in the Newton process (left panel), especially when the network starts to form. We do not report on the final values of the energy functional and the state of  $\|\mathbb{C}\|$  since the differences are minimal with this configuration.

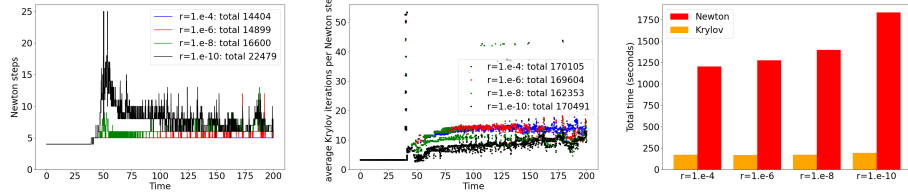


FIGURE 10. BE solver: Newton steps (left panel), average number of linear iterations per Newton step (center), and timings (right) for 4096x4096 mesh with different values of  $r$ . See section 4.5 for additional details.

**4.6. Mesh dependent solutions.** In this Section, we report numerical results using the backward Euler solver and the same model parameters as in section 4.3, comparing triangular and unstructured quadrilateral meshes of the unit domain, in particular:

- **quad structured:** a 512x512 mesh of quadrilaterals,
- **quad unstructured:** an unstructured mesh of 232K quadrilaterals,
- **triangle criss-cross:** the quad-structured mesh where each quadrilateral is split into four triangles along its diagonals,
- **triangle regular:** the quad-structured mesh where each quadrilateral is split into two triangles along one diagonal,
- **triangle irregular:** a completely unstructured mesh with 300K triangles.

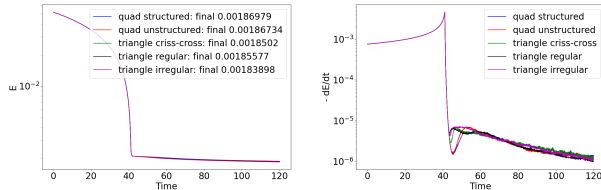


FIGURE 11. Energy (left) and  $-\frac{\partial E}{\partial t}$  (right) as a function of simulation time for different meshes. See section 4.6 for additional details.

All simulations achieve very similar final energy values, with the energy always decaying; see fig. 11. The final states of the norm of the conductivity matrix are shown in fig. 12; the mesh dependence of the final state is evident. While the structured meshes (quad structured, triangle criss-cross, and triangle regular) all lead to similar and symmetric final patterns, the unstructured meshes generate a more irregular network structure. Moreover, all triangular meshes are characterized by a checkerboard distribution of  $\|\mathbb{C}\|$  as shown in the close-ups in fig. 12. Such

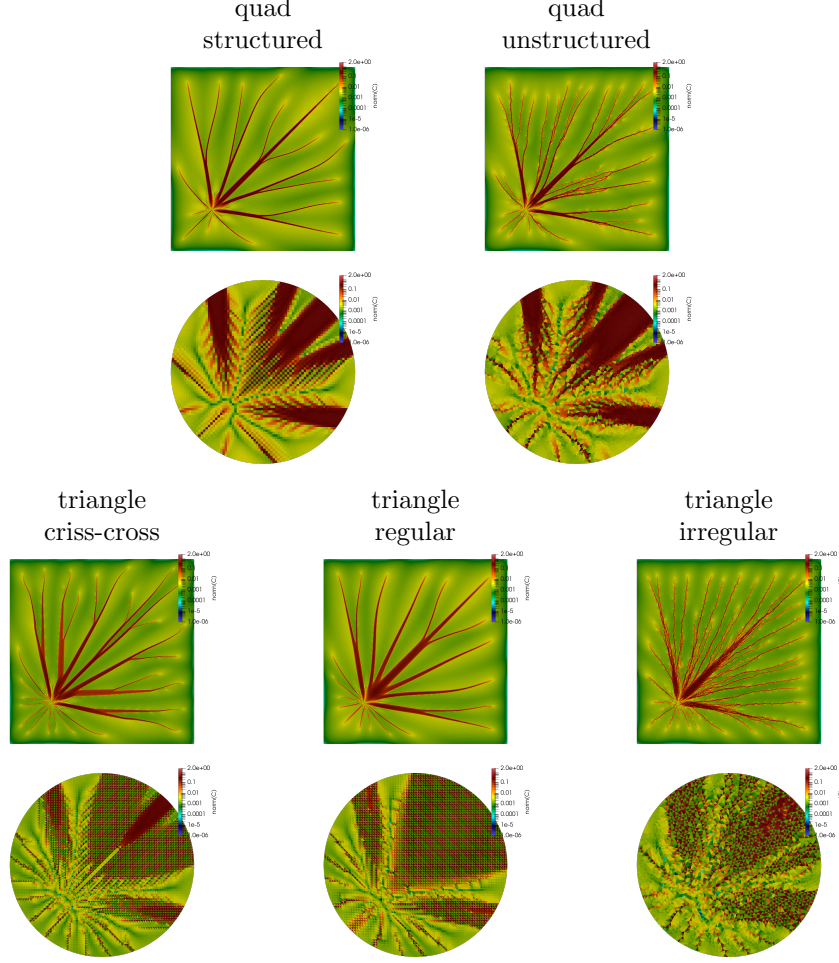


FIGURE 12. Final state of  $\|C\|$  and close-ups at the source location for different meshes as labeled on top. See section 4.6 for additional details.

patterns cannot be resolved by subsequent mesh refinements (data not shown), indicating it is a feature inherent in the discretization.

**4.7. Leaf-based runs with varying  $\gamma$ .** Here, we discuss numerical simulations using the backward Euler solver and the same model parameters as in section 4.3, while considering different values for  $\gamma$ ; specifically,  $\gamma = 0.75$ , and  $\gamma = 0.5$ . Results use the triangular leaf mesh shown in fig. 1, uniformly refined five times for a total of 13 million triangles and 46 million degrees of freedom. The final state of the norm of the conductivity matrix is reported in fig. 13, while macroscopic quantities related to the nonlinear solver are shown in fig. 14.

The final network structure is symmetric with respect to the bisector of the domain in both cases since the mesh has been designed to preserve such symmetry. In the  $\gamma = 0.5$  case, the structure presents smaller ramifications and larger zones

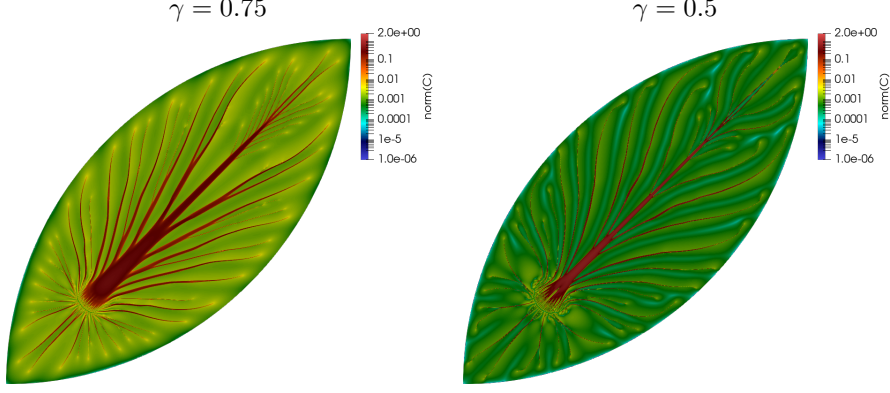


FIGURE 13. Final state of  $\|\mathbb{C}\|$  for different values of  $\gamma$  as labeled on top. See section 4.7 for additional details.

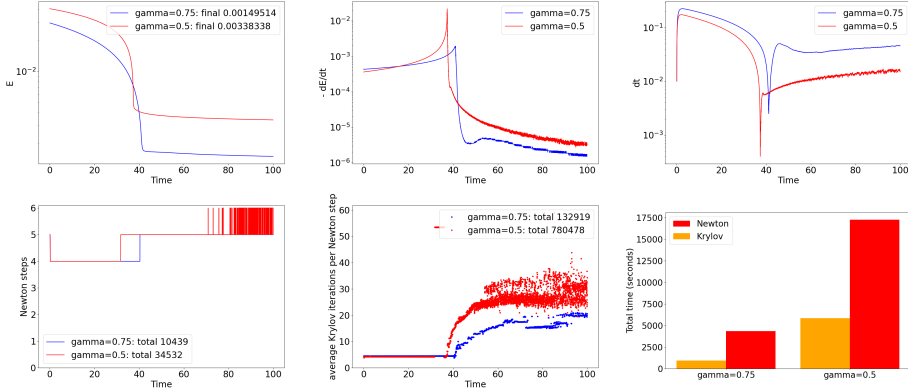


FIGURE 14. Top row: energy (left),  $-\frac{\partial E}{\partial t}$  (center), and time-step (right) as a function of simulation time for different values of  $\gamma$  as indicated in the legends. Bottom row: Newton steps (left panel), average number of linear iterations per Newton step (center), and timings (right). See section 4.7 for additional details.

characterized by small values of  $\|\mathbb{C}\|$ , due to the stronger influence of the negative term  $-\nu \left( \|\mathbb{C}\|^2 + \varepsilon \right)^{\frac{\gamma-2}{2}} \mathbb{C}$ . For both cases of  $\gamma$  considered, the energy is decreasing, with a smaller steady-state value for the  $\gamma = 0.75$  case; with  $\gamma = 0.5$ , initial energy values are larger, and we can observe a faster transition into the network formation stage. Also, for  $\gamma = 0.5$ , the time steps taken by the solver are smaller due to the skinnier network structure of this case, leading to a larger number of time steps and, thus, larger computational times. In both cases, the number of Newton steps is similar since smaller time steps in the  $\gamma = 0.5$  case lead to more manageable Newton steps, thus counteracting the effects of the stronger nonlinearities; on the other hand, the average number of linear iterations is larger for the  $\gamma = 0.5$  case since the

regularization of the Poisson problem within the Schur complement preconditioner has a smaller positive effect.

**4.8. Three-dimensional results.** We close this Section by presenting our three-dimensional simulation results. Here, we consider a slab domain  $[0, 1] \times [0, 1] \times [0, 0.5]$ , discretized with a hexahedral  $256 \times 256 \times 128$  grid. The parameters of the equations are the same as in the previous results, with the exception of the Poisson regularization term, which is now set to  $r = 1.E-3$ . The source term eq. (15) is sampled at  $(0.25, 0.25, 0.25)$ , and the relative tolerance used to solve the nonlinear equations is  $1.E-12$ . The total number of degrees of freedom is 58 million.

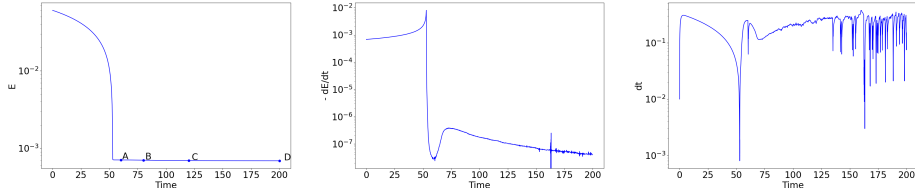


FIGURE 15. Energy (left panel),  $-\frac{\partial E}{\partial t}$  (center), and time step (right), as a function of simulation time for the three-dimensional results. See section 4.8 for additional details.

fig. 15 shows the energy of the system  $E$  (left panel), the negative time derivative of the energy  $-\frac{\partial E}{\partial t}$  (central panel), and the time step  $\delta t$  (right panel) taken by the backward Euler solver. In fig. 16, we report contour plots of  $\|\mathbb{C}\|$  at selected time instances as indicated in the text boxes in fig. 15, while fig. 17 shows the network pattern obtained by isolating the elements where  $\|\mathbb{C}\| > 1.E-2$  only in the half-space  $[0, 1] \times [0, 1] \times [0.25, 0.5]$  since  $\|\mathbb{C}\|$  is symmetric with respect to the plane at  $z = 0.25$ . As in the two-dimensional case, we can again distinguish two stages of the evolution. First, the positive term  $\nabla p \otimes \nabla p$  dominates, and a smooth structure is created (panel A in fig. 16 and in fig. 17). Then, the branching process is triggered, driven by the competition between the above positive term and the negative metabolic term. The branches then propagate through the computational domain. We observe that, similarly as in the two-dimensional case, the branches in three dimensions are essentially one-dimensional structures.

The number of nonlinear iterations per time step and the average number of linear iterations per Newton step are shown in fig. 18. The nonlinearity of the problem is more severe in the late phases of network formation (left panel), while the Schur-complement preconditioner proved to be robust also in the three-dimensional setting (right).

## 5. CONCLUSIONS

We have developed robust and scalable fully implicit nonlinear finite element solvers for simulating biological transportation networks arising from the minimization of a non-convex energy cost functional. Key components of this work are the discretization of the conductivity matrix using a piecewise constant discontinuous space, and the design of robust preconditioners for the linearized systems arising within the Newton method.

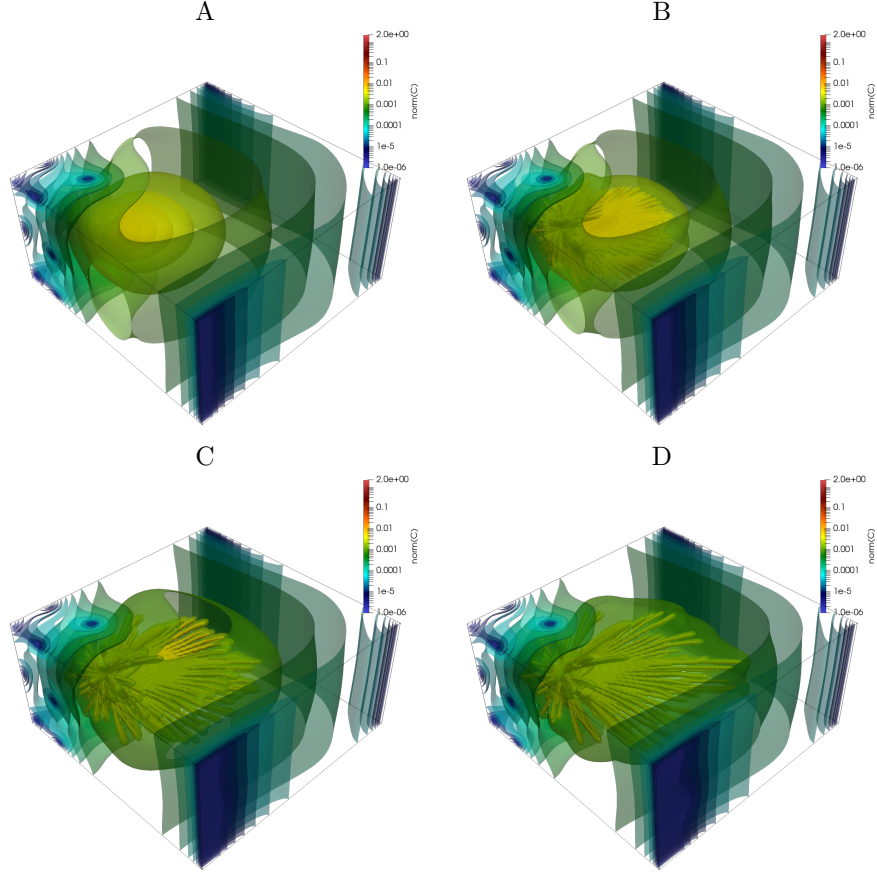


FIGURE 16. Contour plots of  $\|C\|$  at selected time instances as indicated in the text boxes in fig. 15. See section 4.8 for additional details.

The effectiveness of our approach is supported by extensive testing in two and three dimensions, demonstrating the efficiency of the distributed-memory implementation, the robustness of the fully implicit solver, and the algorithmic scalability of the Schur complement preconditioner.

We have shown that the backward Euler time integration scheme successfully preserves the positive semi-definiteness of the conductivity matrix. Furthermore, numerical evidence suggests that solution symmetries (but not positive semi-definiteness) can also be maintained using alternative time-stepping methods such as BDF2 and Crank–Nicolson.

Our results demonstrate, for the first time, the successful simulation of the network formation system in three dimensions. We observe that the key qualitative features of network formation persist in three dimensions, with the emergence of one-dimensional branching structures. The distributed-memory implementation efficiently handles the increased computational complexity, highlighting the feasibility of large-scale three-dimensional simulations for biological transport networks.

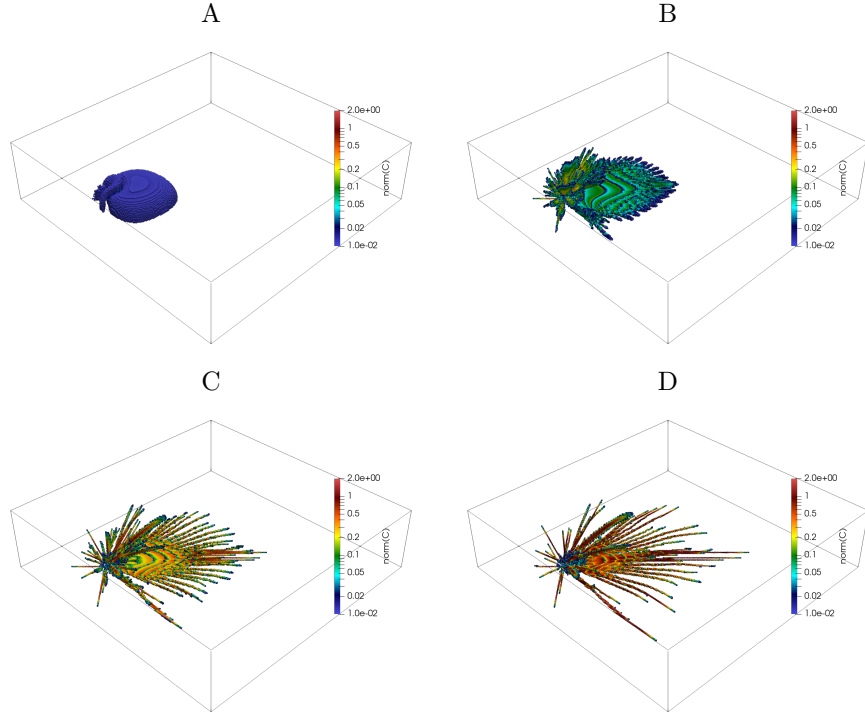


FIGURE 17. Threshold plot  $\|C\| > 1.E-2$  on the half-space  $[0, 1] \times [0, 1] \times [0.25, 0.5]$  at selected time instances as indicated in the text boxes in fig. 15. See section 4.8 for additional details.

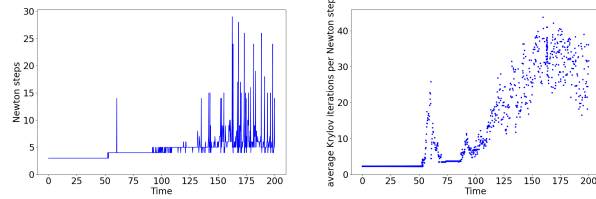


FIGURE 18. Newton steps (left panel) and the average number of linear iterations per Newton step (right) as a function of simulation time for the three-dimensional results. See section 4.8 for additional details.

These findings open the door for further exploration of three-dimensional network formation models in biological and other physical systems.

Numerical experiments revealed a strong dependence of the network structures on the underlying computational mesh, particularly when using triangular elements. We attribute this sensitivity to the choice of an  $H^1(\Omega)$ -conforming space to discretize the pressure field, specifically to its weak approximation properties for the

numerical flux and mass conservation. To address this, we intend to explore a three-field formulation based on a mixed formulation of the Poisson problem in future work.

#### ACKNOWLEDGEMENTS

The research reported in this paper was funded by King Abdullah University of Science and Technology. We are thankful for the computing resources of the Supercomputing Laboratory at King Abdullah University of Science and Technology and, in particular, the Shaheen3 supercomputer

#### REFERENCES

- [1] Shrirang Abhyankar, Jed Brown, Emil M Constantinescu, Debojyoti Ghosh, Barry F Smith, and Hong Zhang. PETSc/TS: A modern scalable ODE/DAE solver library. *arXiv preprint arXiv:1806.01437*, 2018.
- [2] Mark Adams, Marian Brezina, Jonathan Hu, and Ray Tuminaro. Parallel multigrid smoothing: polynomial versus Gauss-Seidel. *Journal of Computational Physics*, 188(2):593–610, 2003.
- [3] Giacomo Albi, Marco Artina, Massimo Foransier, and Peter A. Markowich. Biological transportation networks: Modeling and simulation. *Analysis and Applications*, 14(01):185–206, 2016.
- [4] Giacomo Albi, Martin Burger, Jan Haskovec, Peter Markowich, and Matthias Schlottbom. Continuum modelling of biological network formation. In P. Degond N. Bellomo and E. Tadmor, editors, *Active Particles Vol.I - Theory, Models, Applications*, Modeling and Simulation in Science, Engineering and Technology, pages 1–48. Birkhäuser-Springer, 2017.
- [5] Luigi Ambrosio, Nicola Gigli, and Giuseppe Savaré. *Gradient flows: in metric spaces and in the space of probability measures*. Springer Science & Business Media, 2008.
- [6] Uri M Ascher and Linda R Petzold. *Computer methods for ordinary differential equations and differential-algebraic equations*. SIAM, 1998.
- [7] Clarissa Astuto, Daniele Boffi, and Fabio Credal. Finite element discretization of a biological network formation system: a preliminary study. *XVI International Conference on Hyperbolic Problems: Theory, Numerics, Applications*, pages 247–257, 2022.
- [8] Clarissa Astuto, Daniele Boffi, Jan Haskovec, Peter Markowich, and Giovanni Russo. Comparison of two aspects of a PDE model for biological network formation. *Mathematical and Computational Applications*, 27(5), 2022.
- [9] Clarissa Astuto, Daniele Boffi, Jan Haskovec, Peter Markowich, and Giovanni Russo. Asymmetry and condition number of an elliptic-parabolic system for biological network formation. *Communications on Applied Mathematics and Computation*, pages 1–17, 2023.
- [10] Clarissa Astuto, Jan Haskovec, Peter Markowich, and Simone Portaro. Self-regulated biological transportation structures with general entropy dissipations, part I: The 1D case. *Journal of Dynamics and Games*, 11(1):76–99, 2023.
- [11] Clarissa Astuto, Peter Markowich, Simone Portaro, and Giovanni Russo. Self-regulated biological transportation structures with general entropy dissipation: 2d case and leaf-shaped domain. *arXiv preprint arXiv:2408.15680*, 2024.
- [12] Satish Balay, Shrirang Abhyankar, Mark F. Adams, Steven Benson, Jed Brown, Peter Brune, Kris Buschelman, Emil Constantinescu, Lisandro Dalcin, Alp Dener, Victor Eijkhout, Jacob Faibussowitsch, William D. Gropp, Václav Hapla, Tobin Isaac, Pierre Jolivet, Dmitry Karpeev, Dinesh Kaushik, Matthew G. Knepley, Fande Kong, Scott Kruger, Dave A. May, Lois Curfman McInnes, Richard Tran Mills, Lawrence Mitchell, Todd Munson, Jose E. Roman, Karl Rupp, Patrick Sanan, Jason Sarich, Barry F. Smith, Hansol Suh, Stefano Zampini, Hong Zhang, Hong Zhang, and Junchao Zhang. PETSc/TAO users manual. Technical Report ANL-21/39 - Revision 3.22, Argonne National Laboratory, 2024.
- [13] Satish Balay, Shrirang Abhyankar, Mark F. Adams, Steven Benson, Jed Brown, Peter Brune, Kris Buschelman, Emil M. Constantinescu, Lisandro Dalcin, Alp Dener, Victor Eijkhout, Jacob Faibussowitsch, William D. Gropp, Václav Hapla, Tobin Isaac, Pierre Jolivet, Dmitry Karpeev, Dinesh Kaushik, Matthew G. Knepley, Fande Kong, Scott Kruger, Dave A. May,

Lois Curfman McInnes, Richard Tran Mills, Lawrence Mitchell, Todd Munson, Jose E. Roman, Karl Rupp, Patrick Sanan, Jason Sarich, Barry F. Smith, Stefano Zampini, Hong Zhang, Hong Zhang, and Junchao Zhang. PETSc Web page. <https://petsc.org/>, 2024.

- [14] Satish Balay, William D. Gropp, Lois Curfman McInnes, and Barry F. Smith. Efficient management of parallelism in object oriented numerical software libraries. In E. Arge, A. M. Bruaset, and H. P. Langtangen, editors, *Modern Software Tools in Scientific Computing*, pages 163–202. Birkhäuser Press, 1997.
- [15] Marc Barthélémy. Spatial networks. *Physics reports*, 499(1-3):1–101, 2011.
- [16] Marc Bernot, Vicent Caselles, and Jean-Michel Morel. *Optimal transportation networks: models and theory*, volume 1955. Springer Science & Business Media, 2009.
- [17] Jack Betteridge, Patrick E Farrell, Matthias Hochsteger, Christopher Lackner, Joachim Schöberl, Stefano Zampini, and Umberto Zerbinati. ngsPETSc: A coupling between NETGEN/NGSolve and PETSc. *Journal of Open Source Software*, 9(104):7359, 2024.
- [18] S Bohn, B Andreotti, S Douady, J Munzinger, and Y Couder. Constitutive property of the local organization of leaf venation networks. *Physical Review E*, 65(6):061914, 2002.
- [19] Philippe G Ciarlet. *The finite element method for elliptic problems*. SIAM, 2002.
- [20] Lorenzo Dello Schiavo, Jan Maas, and Francesco Pedrotti. Local conditions for global convergence of gradient flows and proximal point sequences in metric spaces. *Transactions of the American Mathematical Society*, 377(06):3779–3804, 2024.
- [21] Stanley C Eisenstat and Homer F Walker. Choosing the forcing terms in an inexact Newton method. *SIAM Journal on Scientific Computing*, 17(1):16–32, 1996.
- [22] Di Fang, Shi Jin, Peter Markowich, and Benoit Perthame. Implicit and Semi-implicit Numerical Schemes for the Gradient Flow of the Formation of Biological Transport Networks. *The SMAI journal of computational mathematics*, 5:229–249, 2019.
- [23] Istvan Farago and Robert Horvath. Discrete maximum principle and adequate discretizations of linear parabolic problems. *SIAM Journal on Scientific Computing*, 28(6):2313–2336, 2006.
- [24] Charles William Gear. The numerical integration of ordinary differential equations. *Mathematics of Computation*, 21(98):146–156, 1967.
- [25] Volker Grimm, Robert I McLachlan, David I McLaren, GRW Quispel, and Carola-Bibiane Schönlieb. Discrete gradient methods for solving variational image regularisation models. *Journal of Physics A: Mathematical and Theoretical*, 50(29):295201, 2017.
- [26] Jan Haskovec, Lisa Maria Kreusser, and Peter Markowich. ODE and PDE based modeling of biological transportation networks. *arXiv preprint arXiv:1805.08526*, 2018.
- [27] Jan Haskovec, Peter Markowich, and Benoit Perthame. Mathematical analysis of a PDE system for biological network formation. *Communications in Partial Differential Equations*, 40(5):918–956, 2015.
- [28] Jan Haskovec, Peter Markowich, Benoît Perthame, and Matthias Schlottbom. Notes on a PDE system for biological network formation. *Nonlinear Analysis*, 138:127–155, 2016.
- [29] Jan Haskovec, Peter Markowich, and Giulia Pilli. Tensor PDE model of biological network formation. *Communications in Mathematical Sciences*, 20(4):1173–1191, 2022.
- [30] Jan Haskovec, Peter Markowich, and Simone Portaro. Emergence of biological transportation networks as a self-regulated process. *Discrete and Continuous Dynamical Systems*, 43(3,4):1499–1515, 2022.
- [31] Jan Haskovec, Peter Markowich, and Simone Portaro. Measure-based approach to mesoscopic modeling of optimal transportation networks. *arXiv preprint arXiv:2401.07922*, 2024.
- [32] Jan Haskovec and Jan Vybíral. Robust network formation with biological applications. *Networks and heterogeneous media*, 19:791–819, 2024.
- [33] Qi Hong, Jia Zhao, and Qi Wang. Energy-production-rate preserving numerical approximations to network generating partial differential equations. *Computers & Mathematics with Applications*, 84:148–165, 2021.
- [34] Dan Hu. Optimization, adaptation, and initialization of biological transport networks. *Notes from lecture*, 1:3–1, 2013.
- [35] Dan Hu and David Cai. Adaptation and optimization of biological transport networks. *Physical review letters*, 111(13):138701, 2013.
- [36] Eleni Katifori, Gergely J Szöllösi, and Marcelo O Magnasco. Damage and fluctuations induce loops in optimal transport networks. *Physical review letters*, 104(4):048704, 2010.
- [37] Robert C Kirby. Fast simplicial finite element algorithms using Bernstein polynomials. *Numerische Mathematik*, 117(4):631–652, 2011.

- [38] Matthew G Knepley, Jed Brown, Karl Rupp, and Barry F Smith. Achieving high performance with unified residual evaluation. *arXiv preprint arXiv:1309.1204*, 2013.
- [39] Michael Lange, Matthew G Knepley, and Gerard J Gorman. Flexible, scalable mesh and data management using petsc dmplex. In *Proceedings of the 3rd International Conference on Exascale Applications and Software*, pages 71–76, 2015.
- [40] Benoit Merlet and Morgan Pierre. Convergence to equilibrium for the backward euler scheme and applications. *Convergence*, 2009.
- [41] Alexander Mielke. An introduction to the analysis of gradients systems. *arXiv preprint arXiv:2306.05026*, 2023.
- [42] Malcolm F Murphy, Gene H Golub, and Andrew J Wathen. A note on preconditioning for indefinite linear systems. *SIAM Journal on Scientific Computing*, 21(6):1969–1972, 2000.
- [43] Cecil D Murray. The physiological principle of minimum work: I. the vascular system and the cost of blood volume. *Proceedings of the National Academy of Sciences*, 12(3):207–214, 1926.
- [44] Jorge Nocedal and Stephen J Wright. *Numerical optimization*. Springer, 1999.
- [45] Christopher C Paige and Michael A Saunders. Solution of sparse indefinite systems of linear equations. *SIAM journal on numerical analysis*, 12(4):617–629, 1975.
- [46] Simone Portaro. A mathematical journey through biological optimal transportation networks. *Doctoral thesis, King Abdullah University of Science and Technology*, 2024.
- [47] Youcef Saad and Martin H Schultz. GMRES: A generalized minimal residual algorithm for solving nonsymmetric linear systems. *SIAM Journal on scientific and statistical computing*, 7(3):856–869, 1986.
- [48] Filippo Santambrogio. {Euclidean, metric, and Wasserstein} gradient flows: an overview. *Bulletin of Mathematical Sciences*, 7:87–154, 2017.
- [49] Gustaf Söderlind. Digital filters in adaptive time-stepping. *ACM Transactions on Mathematical Software (TOMS)*, 29(1):1–26, 2003.
- [50] Atsushi Tero, Seiji Takagi, Tetsu Saigusa, Kentaro Ito, Dan P Bebber, Mark D Fricker, Kenji Yumiki, Ryo Kobayashi, and Toshiyuki Nakagaki. Rules for biologically inspired adaptive network design. *Science*, 327(5964):439–442, 2010.
- [51] Jinchao Xu and Ludmil Zikatanov. Algebraic multigrid methods. *Acta Numerica*, 26:591–721, 2017.
- [52] Lei Yang, Yuan Liu, Yan Jiang, and Mengping Zhang. Discontinuous galerkin methods for network patterning phase-field models. *Journal of Scientific Computing*, 98(1):27, 2024.
- [53] Stefano Zampini. PCBDDC: a class of robust dual-primal methods in PETSc. *SIAM Journal on Scientific Computing*, 38(5):S282–S306, 2016.
- [54] Stefano Zampini. Instructions to reproduce the results of the paper "robust and scalable nonlinear solvers for finite element discretizations of biological transportation networks", April 2025.